Supplementary Information (SI) for Journal of Materials Chemistry C.

Suppression of phase segregation in CsPbIBr2-based perovskites red LEC/LED: impact of Mn doping, crystallization control, and grain passivation

Andrei S. Toikka, Ramazan Kenesbay, Maria Baeva, Dmitry M. Mitin, Maria Sandzhieva, Aleksandr Goltaev, Vladimir Fedorov, Alexander Pavlov, Dmitry Gets, Ivan Mukhin and Sergei Makarov

Supplementary Information

Optimization of Mn-doping and thermal treatment

Fixed parameters: 0.4 molar perovskite concentration, perovskite:(PEO+PVDF):LiTFSi mass ratio – 1:0.1:0.01; PEO:PVDF mass ratio – 1:9; spin-coating – 1000 rpm for 60 s; vacuuming temperature – 60 ˚C. Variable parameters: stoichiometry of $CsPb_{1-x}Mn_xIBr_2$ ($0 \leq x \leq 0.1$), annealing temperature 60-70°C (for x=0) and 70-80°C (for x>0).

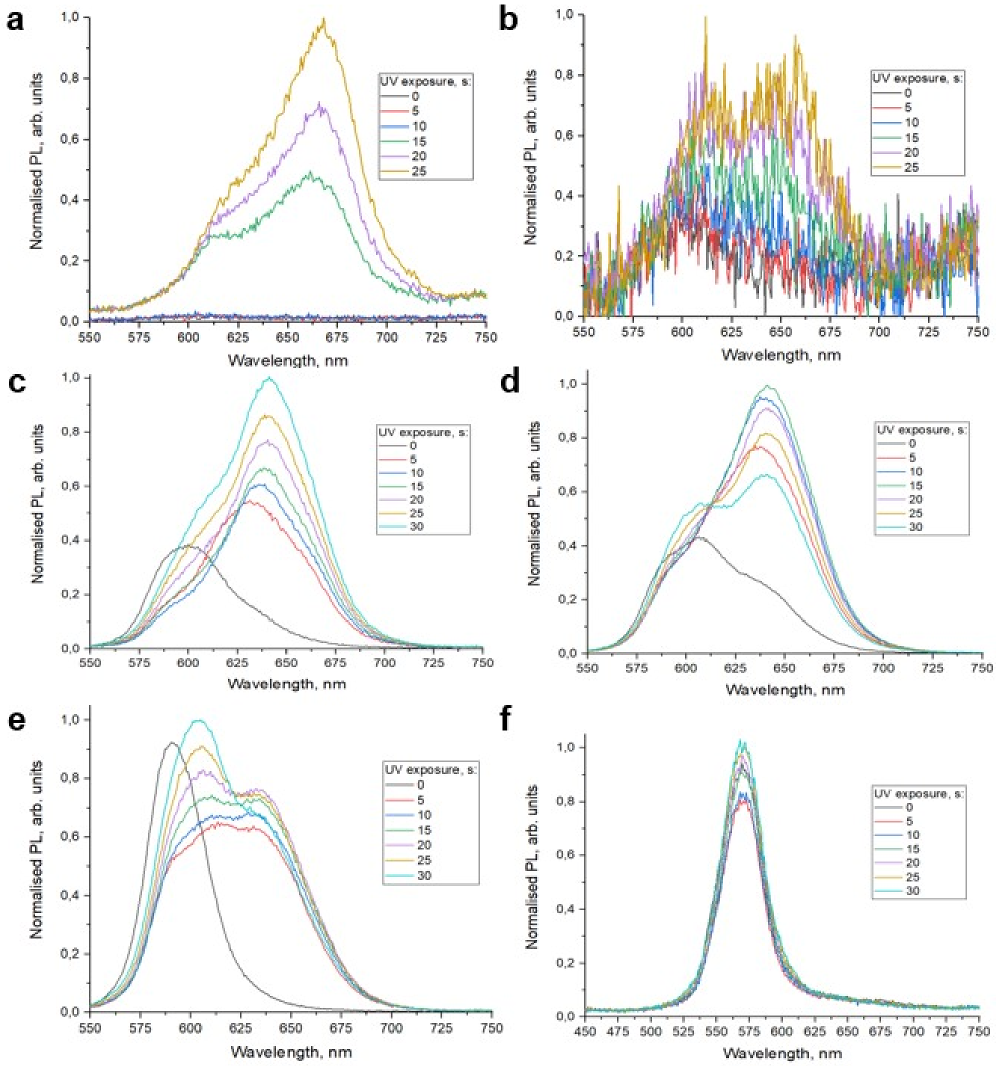

Fig. S1. Normalized PL flux temporal dependencies of perovskite-based structures with various content of Mn and annealing temperature: 0 wt. % - 60˚C (a) and 70˚C (b); 5 wt. % - 70˚C (c) and 80˚C (d); 10 wt. % - 70˚C (e) and 80˚C (f)

PL intensity is limited due to the defects, in particular with the formation of Br-rich areas (Fig.S2(c-f)).

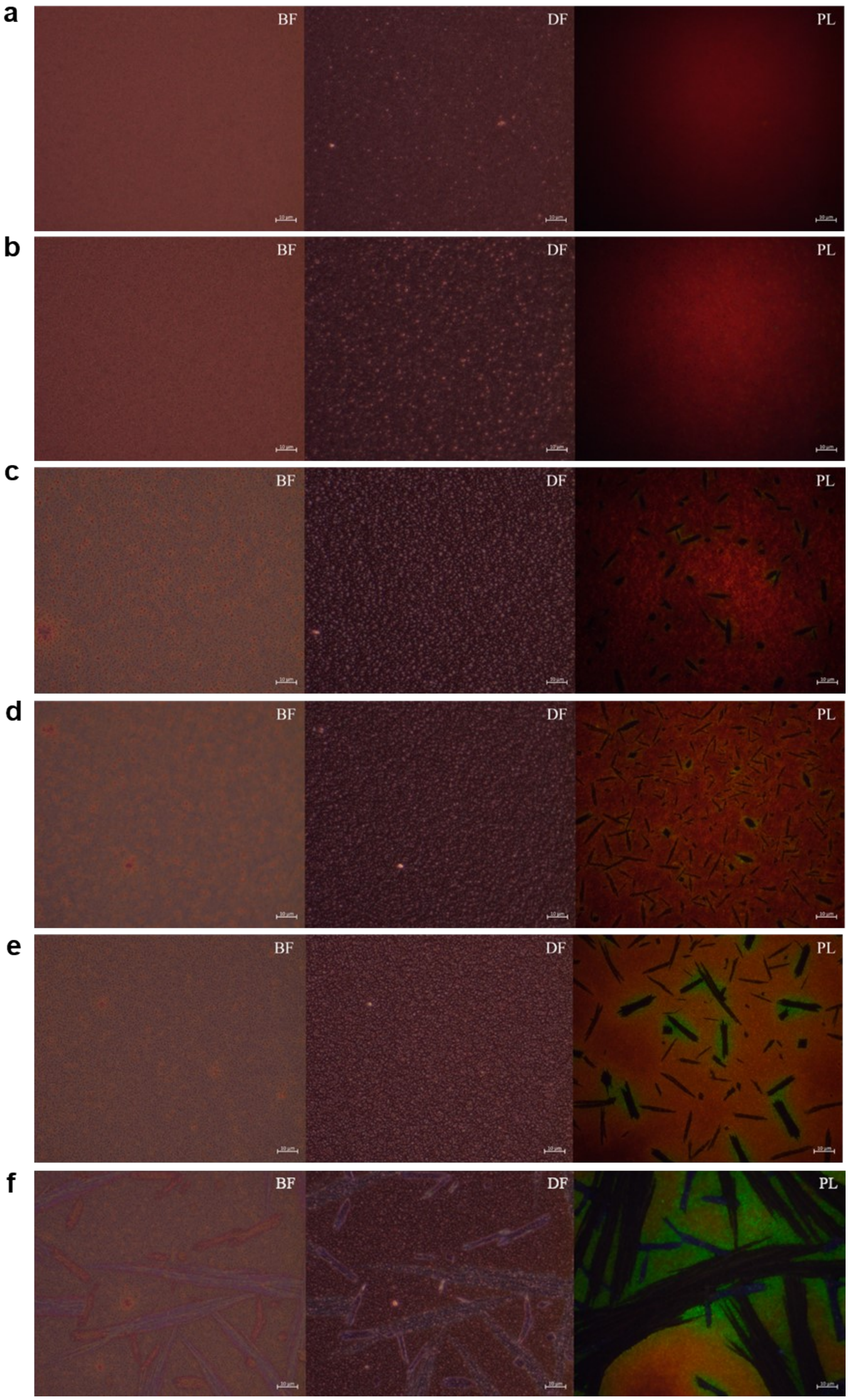

Fig. S2. Optical microscopy in bright field (BF), dark field (DF), photoluminescence (PL) mode of perovskite-based structures with various content of Mn and annealing temperature: 0 wt. % - 60˚C (a) and 70˚C (b); 5 wt. % - 70˚C (c) and 80˚C (d); 10 wt. % - 70˚C (e) and 80˚C (f)

PL images of samples without Mn doping don't reveal Br-rich areas due to the small PL intensity. However, PL spectral measurements (Fig. S1(a,b)) demonstrate this aspect.

Thus, based on the required PL peak's position and FWHM, regimes with Mn content (5 wt. %) and annealing temperatures of (70-80˚C) are optimal in this series. The further optimization was provided by searching for PEO/PVDF optimal ratio.

Spectrophotometry and Tauc plot

Spectral dependencies of OD were measured directly via spectrophotometer. This parameter demonstrates the relationship between incident (Φ_{in}) and transmitted (Φ_{out}) optical flux respectively [S1]:

$$OD = lg\left(\frac{\Phi_{in}}{\Phi_{out}}\right) = lg\left(\frac{\Phi_{in}}{\Phi_{in}T_{sub}T_{sample}}\right) = - lg\left(T_{sub}T_{sample}\right), \qquad \text{(S1)}$$

where T_{sub} and T_{sample} – transmittance of substrate and sample, respectively.

The conventional method for the determination of optical band gap (E_g^{opt}) is an application of Tauc plot [S2]. According to Tauc's assumption, the absorption coefficient (α) for directly allowed interband transitions could be described near the band edge via the quadratic dependence versus photon energy (E=hʋ):

$$\alpha(h\upsilon)\cdot h\upsilon \sim \left(h\upsilon - E_g^{opt}\right)^{1/2} \qquad \text{(S2)}$$

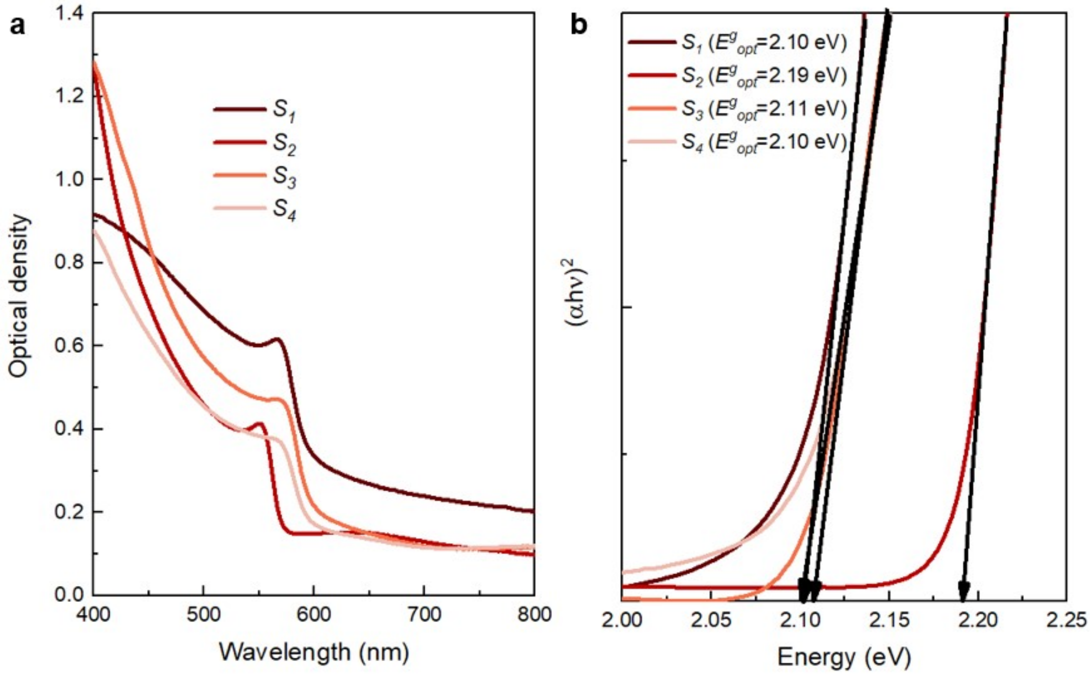

Fig. S3. (a) OD spectral dependencies of CsPbIBr$_2$-based thin films, (b) Tauc plots for S1-S4 samples. Legend shows the estimated band gap values.

Table S1 presents the bandgap value for CsPbIBr$_2$-based and related materials reported in the literature.

Table. S1. The values of band gap for CsPbIBr$_2$-based and related materials

Structure	Band gap (eV)	Comment	Ref.
CsPIbBr$_2$ (thin film)	~2.12 eV (optical)	Tauc plot	[S3]
CsPbIBr$_2$ (nanocrystals)	~2.10 eV (optical)	Tauc plot	[S4]
CsPbIBr$_2$	~2.00 eV	DFT study (mBJ-GGA potential)	[S5]
CsPbIBr$_2$	~2.391 eV (electronic)	DFT study (plane-wave pseudopotential)	[S6]
CsPbIBr$_2$	~2.05 eV	-	[S7]
CsPbIBr$_2$	~2.08 eV	-	[S8]
CsPbIBr$_2$	~2.05 eV	Absorption spectra	[S9]
CsPbIBr$_2$ (nanocrystals)	~2.21 eV (optical)	Tauc plot	[S10]
CsPbIBr$_2$ (thin film)	~2.05 eV (optical)	Tauc plot	[S11]
CsPb$_{0.9}$Mn$_{0.1}$IBr$_2$ (thin film)	~2.02 eV (optical)		
CsPbIBr$_2$ (thin film)	~1.89 eV (optical)	Tauc plot	[S12]
CsPb$_{0.995}$Mn$_{0.00501}$I$_{1.01}$Br$_{1.99}$ (thin film)	~1.85 eV (optical)		
CsPb$_{0.99}$Mn$_{0.01}$I$_{1.02}$Br$_{1.98}$ (thin film)	~1.81 eV (optical)		
CsPb$_{0.98}$Mn$_{0.02}$I$_{1.04}$Br$_{1.96}$ (thin film)	~1.80 eV (optical)		
CsPb$_{0.95}$Mn$_{0.05}$I$_{1.1}$Br$_{1.9}$ (thin film)	~1.80 eV (optical)		

SEM statistics

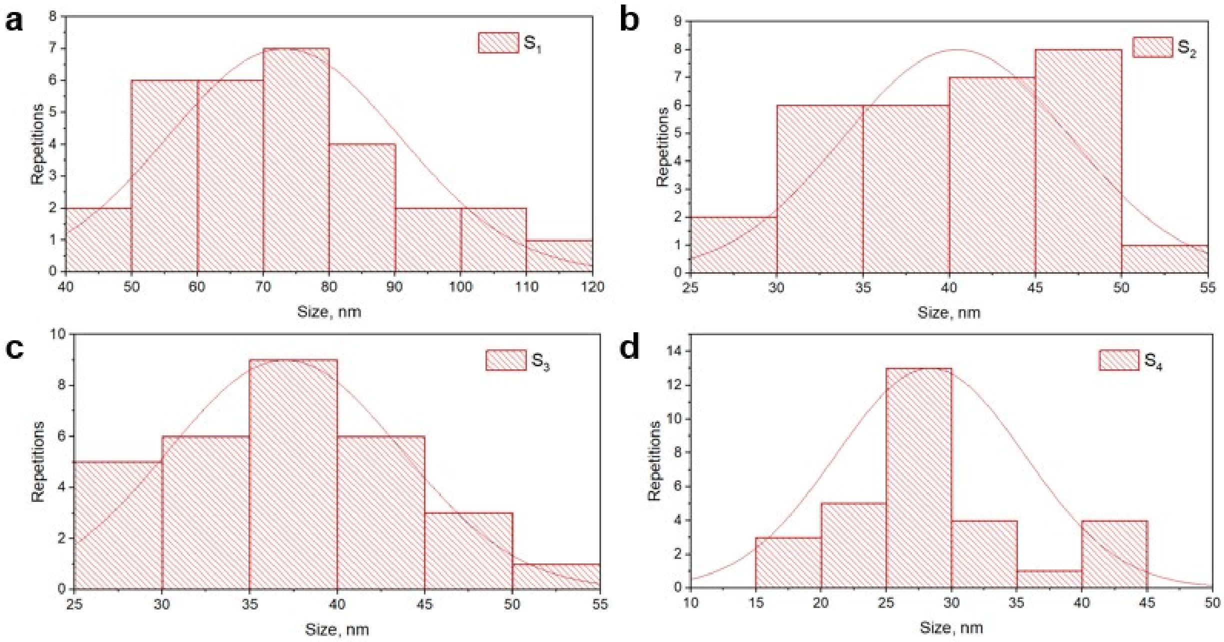

Fig. S4. Crystal grain size distribution for S_1 (a), S_2 (b), S_3 (c), S_4 (d) samples

Table S2. Crystal grain size statistic parameters for S_1-S_4 samples

Crystal grain size	Sample			
	S_1	S_2	S_3	S_4
Mean value (nm)	73	40	37	28
Standard deviation (nm)	18	7	7	7

Optimization of PEO/PVDF content

The fixed parameters: 0.4 molar perovskite concentration, stoichiometry of $CsPb_{1-x}Mn_xIBr_2$ (x=0.05), perovskite:(PEO+PVDF):LiTFSi mass ratio – 1:0.1:0.01, spin-coating – 1000 rpm / 60 s; vacuuming temperature – 60 ˚C, annealing temperature – 70 ˚C. Variable parameters: PEO:PVDF mass ratio (1:0, 1:1, 1:2, 1:4, 1:9). PL intensity was normalized on the PL maximum intensity of the sample without PVDF content. All compared samples had stable PL, however the peak's positions were different (Figure S4). Based on the comparison of PL intensity and peak's position, the regime with PEO:PVDF=1:4 (Figure S4d) was considered to be optimal.

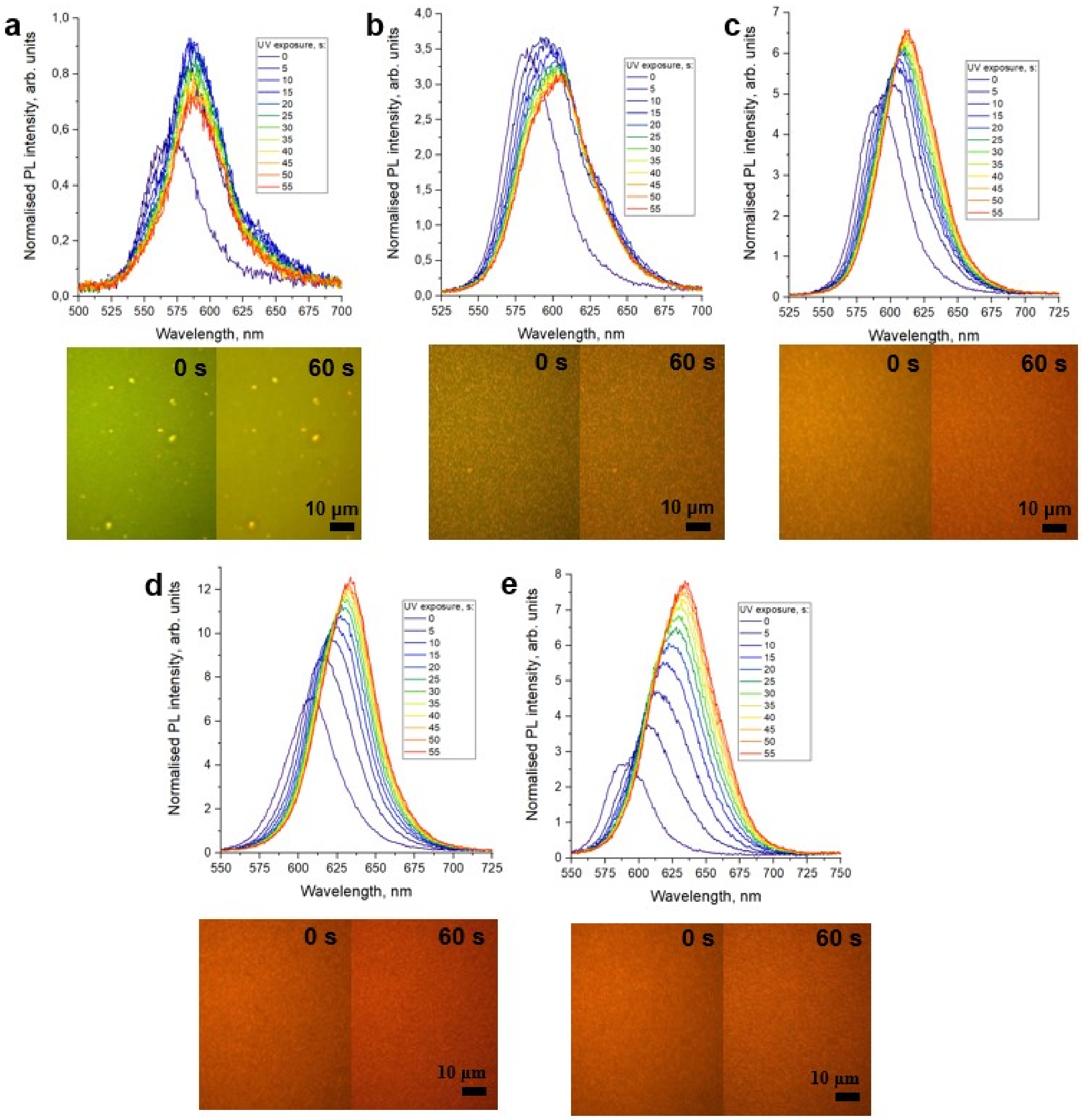

Fig. S5. PL spectra and maps of perovskite-based thin films with the various PEO:PVDF mass ratio and various time of UV exposure: 1:0 (a), 1:1 (b), 1:2 (c), 1:4 (d), 1:9 (e). Labels “0 s” and “60 s” correspond to UV-exposure time of samples during PL measurements.

EDX measurements

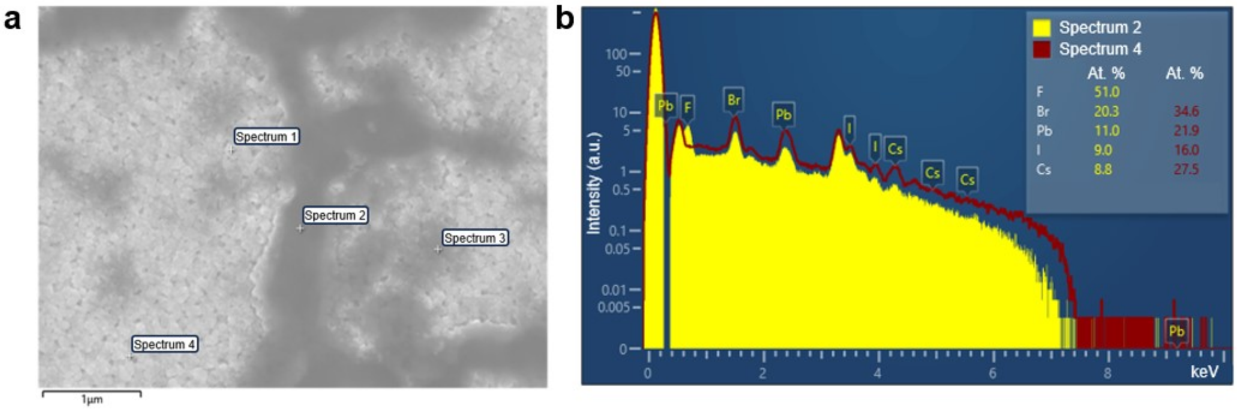

Fig. S6. SEM image of S_1 sample surface (a) and related EDX spectra (b)

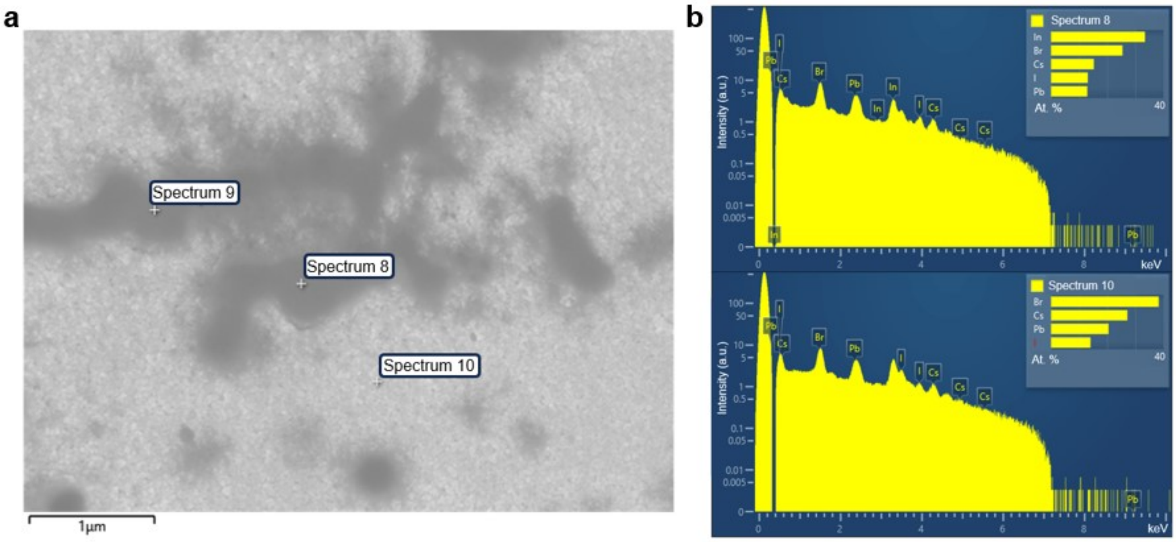

Fig. S7. SEM image of S_2 sample surface (a) and related EDX spectra (b)

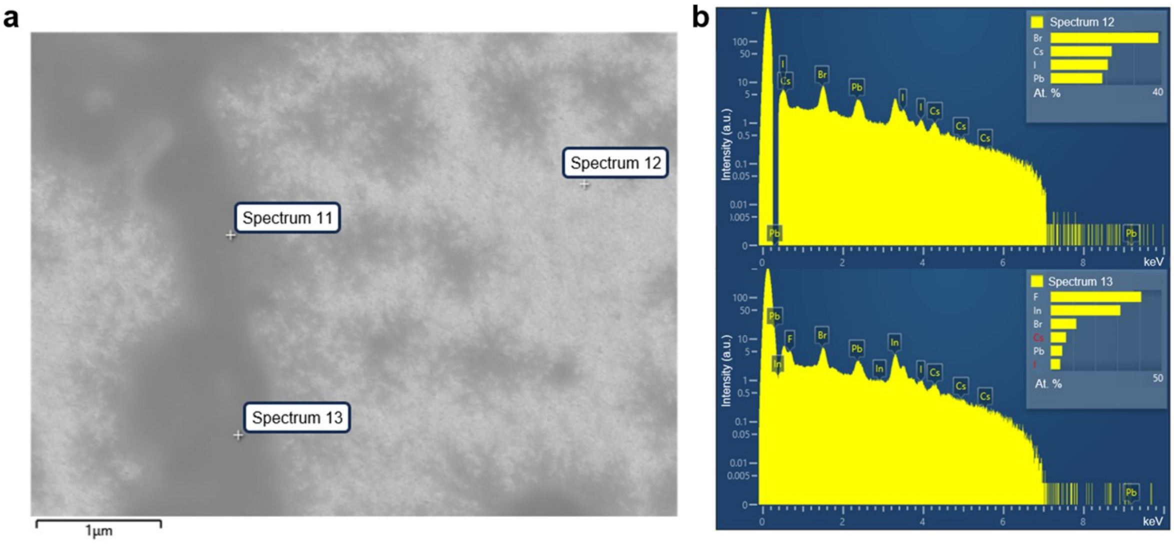

Fig. S8. SEM image of S_3 sample surface (a) and related EDX spectra (b)

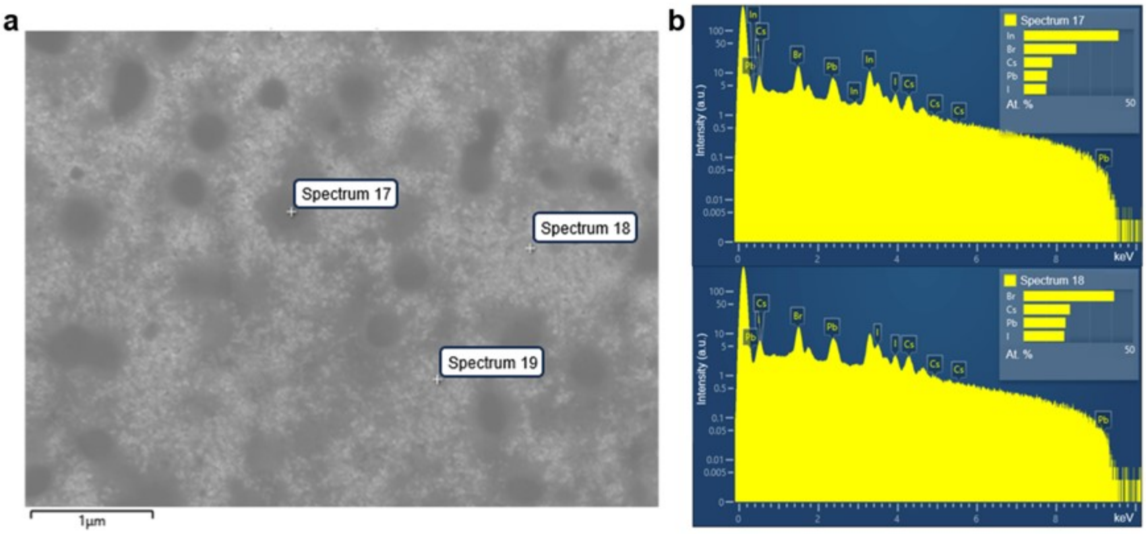

Fig. S9. SEM image of S_4 sample surface (a) and related EDX spectra (b)

Table S3. The acquired Br/I ratio in S_1-S_4 samples (EDX data).

Sample	Br/I ratio					
	Perovskite-rich area			Polymer-rich area		
	Min	Avg	Max	Min	Avg	Max
S_1	2.1	2.1	2.2	3.7	3.8	4.0
S_2	2.7	2.7	2.8	1.8	1.9	2.0
S_3	1.8	1.8	2.0	2.6	2.6	2.7
S_4	2.1	2.1	2.2	2.3	2.4	2.5

Figure S10 shows SEM and EDX results for S_4 sample. The bright regions in the SEM image (see left panel in Figure S10) correspond to the perovskite layer with Mn. The dark regions in the SEM image correspond to organic (F) and Mn-reach areas with low content of perovskite (see right panel in Figure S10). This makes the layer slightly inhomogeneous, however, the average lateral size of these regions doesn't exceed 0.5-1 μm, which does not significantly deteriorate the PL and EL properties of S_4 sample. Moreover, this doesn't lead to perovskite layer phase separation, which is also confirmed by Table S3. Taking into account the results of EL tracking for S_1-S_4 samples (see Figure S16 below and Figure 5 in the main manuscript), we suggest that S_4 receipt is optimal.

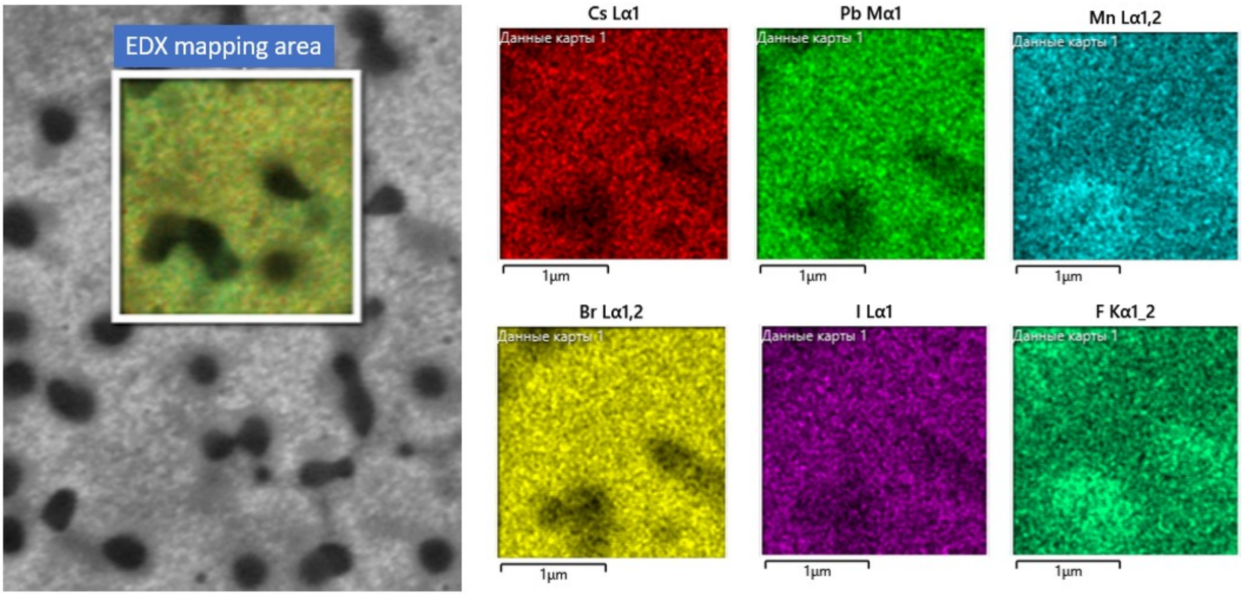

Fig. S10. SEM and EDX elemental mapping of S_4 sample

DFT calculations

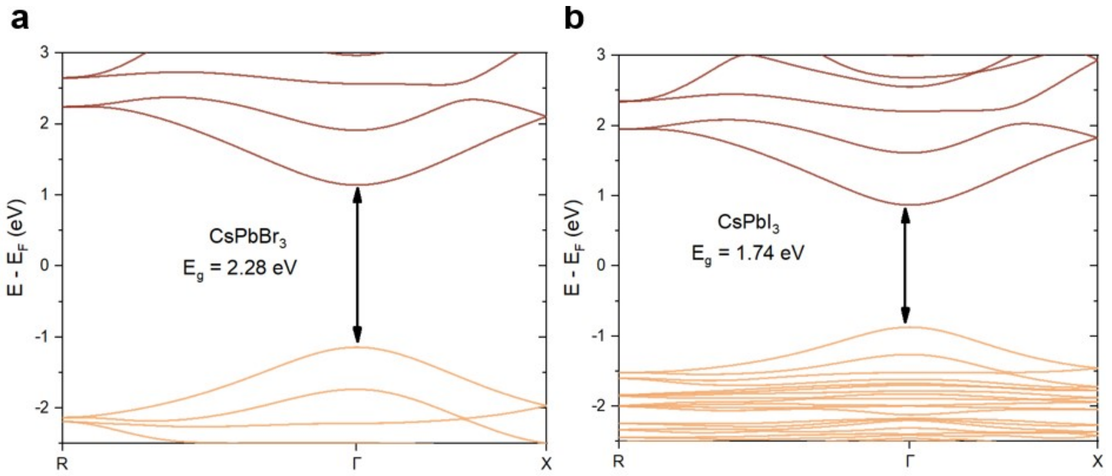

Fig. S11. The energy band structures along high-symmetry points for $CsPbBr_3$ (a) and $CsPbI_3$ (b) calculated using DFT and averaged over 5 random cells. E_F is a Fermi level.

XRD measurements

Figure S12 shows close-up images of the overlapping 040, 224, and 400 Bragg reflections for the S_1 and S_4 samples. One can see that the XRD peak corresponding to samples S_4 is shifted towards larger 2θ angles by 0.1 degree compared to the sample S_1, which is free of Mn doping. This indicates a smaller lattice volume compared to the S_1 sample, which was synthesized without adding Mn.

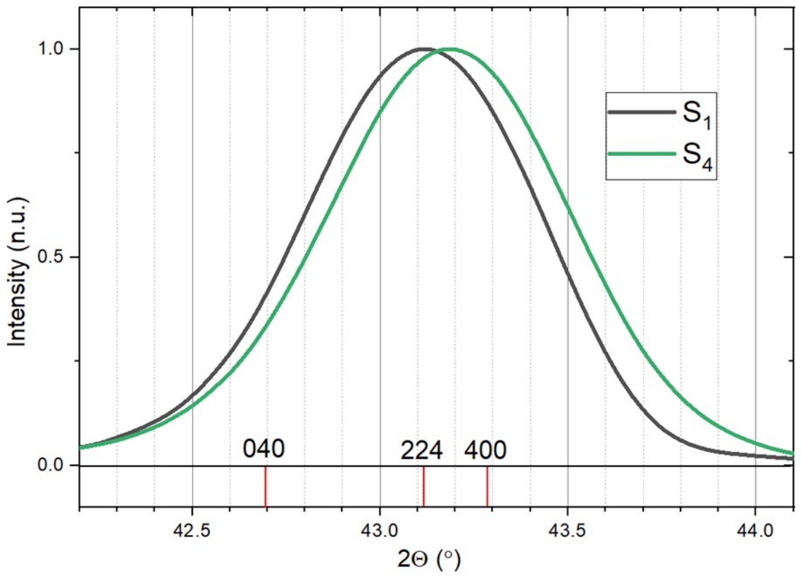

Fig. S12. XRD curves of the studied S_1 and S_4 samples

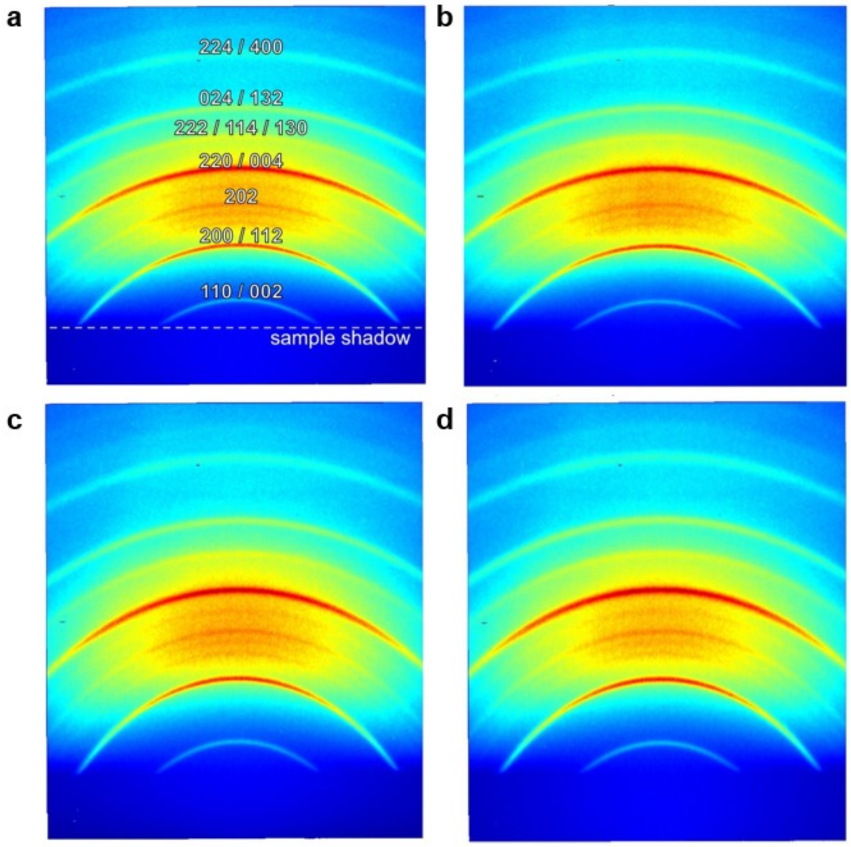

Fig. S13. Raw 2D CCD images of the X-ray diffraction patterns obtained from the synthesized samples: (a) S_1, (b) S_2, (c) S_3, (d) S_4

Table S4. The lattice parameters and the $CsPb(I_xBr_{1-x})_3$ composition obtained from the XRD data according to Vegard's law.

Sample	a (Å)	b (Å)	c (Å)	pseudo-cub $\langle a_{ps\text{-}cub} \rangle$ (Å)	x (%)
S_1	8.365	8.463	11.834	5.939	30
S_2	8.356	8.461	11.829	5.935	29
S_3	8.362	8.467	11.839	5.940	30
S_4	8.362	8.462	11.824	5.936	29

Comparison of PL distributions for samples S_1-S_4

PL images of samples S_1-S_4 (Fig. S2b) were separated by "red-green-blue" (RGB) filters with 8-bit (0 - minimum, 255 - maximum, linear dependence) scale. Results for the red channel are demonstrated below in Fig. S14.

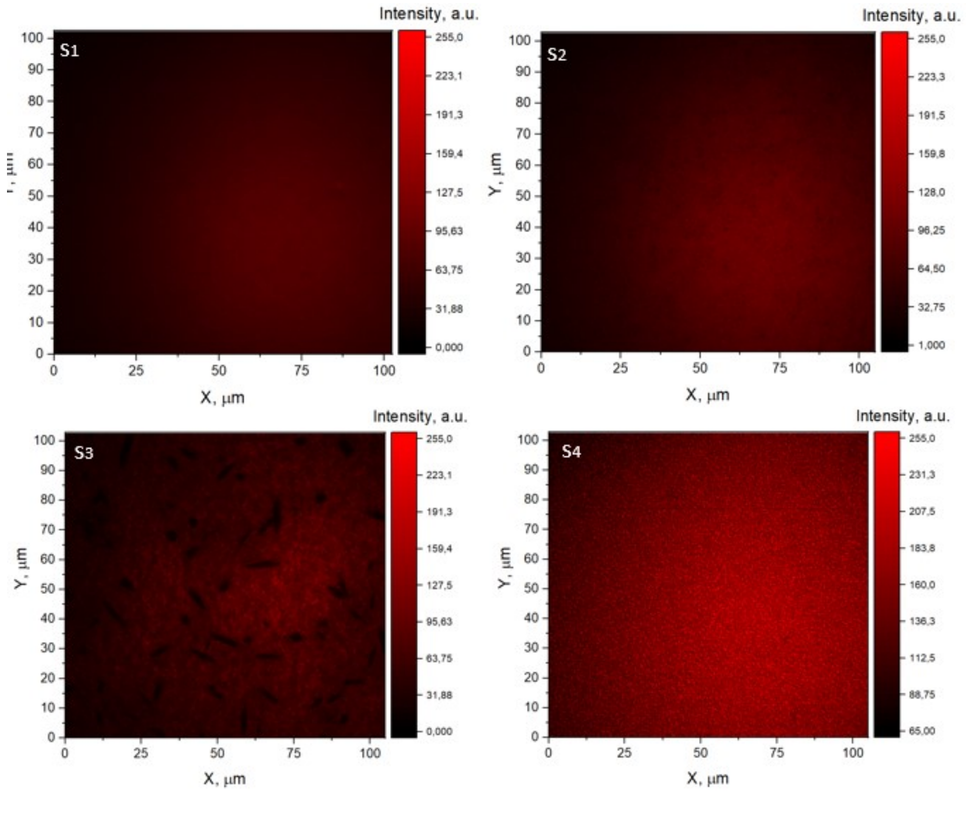

Fig. S14. PL intensity distribution for S_1-S_4 samples versus surface apertures for the "red" channel in RGB 8-bit scale

Intensity distribution of reduced quantity of pixels with intensity I ($N_{pix}(I)$) is demonstrated below. Here, N_{pix}(total) - total quantity of pixels in images of PL.

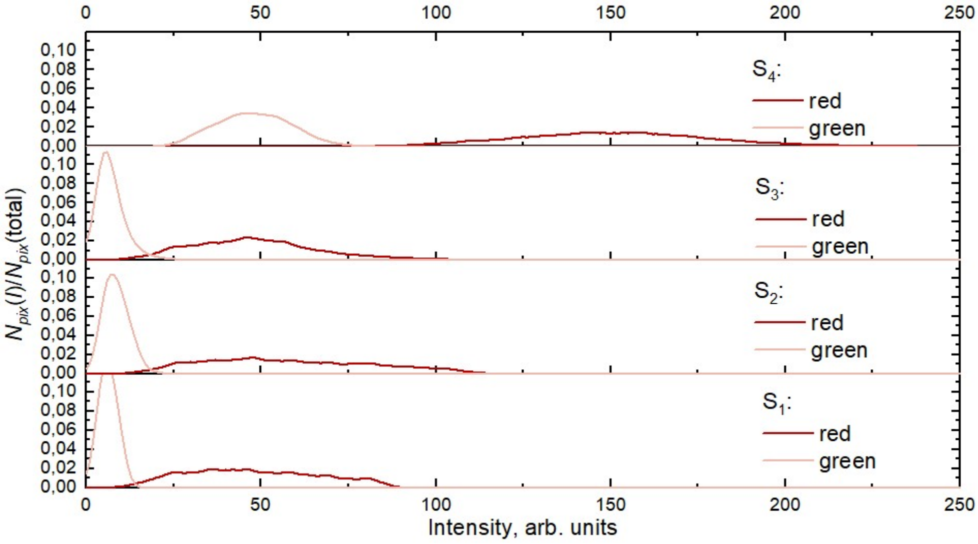

Fig. S15. Distribution of pixel's intensity in PL map of S_1-S_4 for "red" and "green" channels in 8-bit color scale

PeLEC and PeLED device characterization

Figure S16 shows EL time-tracking for S_1-S_3 receipt-based PeLECs. The observed lifetime of control PeLEC (S_1 sample) does not exceed 5 s (Figure S16a). After Mn doping (S_2 receipt), the stability of the device was improved, and the lifetime value increased to 20-25 s (Figure S16b). The additional crystallization control optimization by annealing temperature (receipt S_3) provided the higher EL-signal and stability of PeLEC (Figure S16c). However, the lifetime of this device was less than 1 min. The best results were achieved for S_4 sample (see Figure 4 and 5 in the main manuscript).

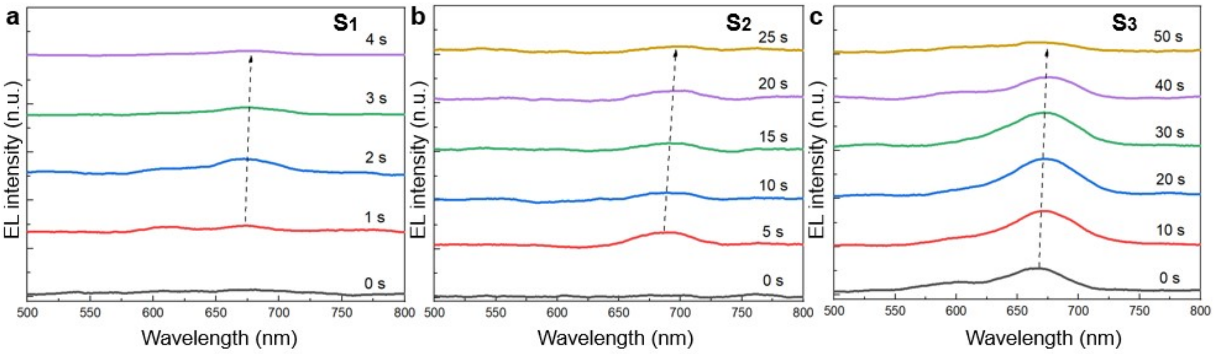

Fig. S16. EL spectra during PeLECs time-tracking with control S_1 (a) and intermediate-optimized receipts S_2 (b), S_3 (c). 0 s correspond to the start of electrical field pumping. Applied bias was 5.5 V

Table S5. Tracking comparison of the developed PeLED and PeLEC devices (based on data from Fig. 5 in manuscript)

$CsPb_{0.95}Mn_{0.05}IBr_2$ (PeLED)		$CsPb_{0.95}Mn_{0.05}IBr_2$ / PEO / PVDF / LiTFSI (PeLEC)	
Time range (min)	Interpretation (dominant mechanism)	Time range (min)	Interpretation (dominant mechanism)
0…0.12	Diffusion of ions (Cs+, I-, Br-) [S13-S14], phase segregation (Figure S14b).	0…1.2	EDL and dynamic p-i-n structure formation [S13, S15] (Figure 5a).
0.12…1.2	Drastic phase segregation of I- and Br- anions with current density rise (Figure S14a), shift and broadening of EL peak (Figure S14b).	1.2…3.6	Due to the formation of EDL the thickness of layer for radiative recombination decreases and the effective electric field strength rises. This regime corresponds to the rise of current density and EL flux (Figure 5a). p-i-n structure was almost completely formed near *t* = 3.6 min, what corresponds to the maximum of EL flux (Figure 5a,b).
>1.2	Under current density > 250 mA/cm^2 breakdown of perovskite was observed. This region corresponds to the dramatic rise of current density (Figure S15a) and drop of EL intensity. EL spectra correspond to the formation of multiple regions with high quantity of defects and various stoichiometry (Figure S14b).	3.6…12	Rise of current density caused by diffusion of ions. In particular, it caused the starting of phase segregation with I- and Br- anions diffusion with corresponding EL shift (Figure 5b). Near *t* = 12 min the value of current density exceeded 250 mA/cm^2 and almost full aperture of pixel was breakdown.

References

[S1] A.N. Matveew (eds). Optics (Mir publishers, 1988).

[S2] Klein, J., et. al. Limitations of the Tauc Plot Method. *Advanced Functional Materials*, **2304523**, 1–19 (2023).

[S3] Li, J., et. al. All-vacuum fabrication of yellow perovskite light-emitting diodes. *Science Bulletin* **67**, 178–185 (2022).

[S4] Pal, S., et. al. Strain mediated light emission using heterojunctions of all-inorganic mixed-halide perovskite nanocrystals via piezo-phototronic effect. *Nano Energy* **106200**, 1–12 (2021).

[S5] Najim, A., et. al. Theoretical investigation of structural, electronic, and optical properties of halide cubic perovskite $CsPbBr_{3-x}I_x$. *Materials Science in Semiconductor Processing* **106442**, 1–9 (2022).

[S6] Maleka, P. M., et. al. Study of inorganic lead halide perovskites properties using first-principles density functional theory for photovoltaic and optoelectronic devices. *Materials Today: Proceedings* **62**, S12–S22 (2022).

[S7] Zhang, C., et. al. Low-Temperature Crystallization of $CsPbIBr_2$ Perovskite for High Performance Solar Cells. *Solar RRL* **2000254**, 1–8 (2020).

[S8] Zhang, H., et. al. Suppressed light-induced phase transition of CsPbBr2I: Strategies, progress and applications in the photovoltaic field. *Journal of Semiconductors* **071901**, 1–13 (2021).

[S9] Zhu, W., et. al. Intermolecular Exchange Boosts Efficiency of Air-Stable, Carbon-Based All-Inorganic Planar $CsPbIBr_2$ Perovskite Solar Cells to Over 9%. *Advanced Energy Materials* **1802080**, 1–9 (2018).

[S10] Suhail, A., et. al. Tuneable structural and optical properties of inorganic mixed halide perovskite nanocrystals. *Applied Research* **e202200095**, 1–9 (2023).

[S11] Zheng, L., et. al. Manganese Doped Perovskite $CsPb_{0.9}Mn_{0.1}Br_2I$ Solar Cells with Enhanced Stability and Reduced Toxicity. *Georgia Journal of Science* **2**, 1–16 (2022).

[S12] Liang, J., et. al. Enhancing Optical, Electronic, Crystalline, and Morphological Properties of Cesium Lead Halide by Mn Substitution for High-Stability All-Inorganic Perovskite Solar Cells with Carbon Electrodes. *Advanced Energy Materials* **1800504**, 1–7 (2018).

[S13] Gets, D., et. al. Reconfigurable Perovskite LEC: Effects of Ionic Additives and Dual Function Devices. *Advanced Optical Materials* **2001715**, 1–21 (2021).

[S14] Mishra, A., et. al. Enhanced Operational Stability of Perovskite Light-Emitting Electrochemical Cells Leveraging Ionic Additives. *Advanced Optical Materials* **2000226**, 1–19 (2020).

[S15] Baeva, M., et. al. ITO-free silicon-integrated perovskite electrochemical cell for light-emission and light-detection. *Opto-electronic advances* **6(220154)**, 1-14 (2023).